Lim, C-S, Levi, E, Jones, M, Abd Rahim, N and Hew, W-P

A Fault-Tolerant Two-Motor Drive With FCS-MP-Based Flux and Torque Control

https://researchonline.ljmu.ac.uk/id/eprint/1658/

Article

Citation (please note it is advisable to refer to the publisher's version if you intend to cite from this work)

Lim, C-S, Levi, E, Jones, M, Abd Rahim, N and Hew, W-P (2014) A Fault-Tolerant Two-Motor Drive With FCS-MP-Based Flux and Torque Control. IEEE TRANSACTIONS ON INDUSTRIAL ELECTRONICS, 61 (12). pp. 6603-6614. ISSN 0278-0046

A Fault-Tolerant Two-Motor Drive with FCS-MP Based Flux and Torque Control

Chee Shen Lim, *Student Member, IEEE*, Emil Levi, *Fellow, IEEE*, Martin Jones, Nasrudin Abd. Rahim, *Senior Member, IEEE*, Wooi Ping Hew, *Member, IEEE*

***Abstract*–Independently controlled multi-motor drives are typically realized by using a common dc link and independent sets of three-phase inverters and motors. In the case of an open-circuit fault in an inverter leg, one motor becomes single-phase. To enable continued controllable operation by eliminating single-phasing, the supply for the motor phase with the faulted inverter leg can be paralleled to a healthy leg of another inverter, using hardware reconfiguration. Hence, the two motors are now supplied from a five-leg inverter, which has inherent voltage and current limitations. Theoretically, violating the voltage limit leads to inverter over-modulation and large torque oscillations. It is shown here that the finite-control-set model predictive control (FCS-MPC), designed to control the machines' stator flux and torque, can consider the inherent voltage limit dynamically in the control loop. Apart from preserving the independent control of the two machines, the additional constraint consideration significantly widens the operating speed ranges of the machines. In particular, it is shown that whenever the voltage limit is entered, the controller reduces the stator flux level automatically, without requiring external flux reference change. The obtained performance is illustrated using experimental results and is also compared to the conventional two-motor field-oriented control scheme. The control concept is thus fully experimentally verified.**

Index Terms — **Two-motor drive, open-circuit fault, model predictive control, flux and torque control, field weakening.**

I. INTRODUCTION

Multi-motor three-phase drives use typically a common dc link and separate three-phase inverters to realize independent motor control. In the case of an open-circuit fault in one of the inverter legs, a possible solution for fault-tolerant operation is to use a switch to connect the motor phase that has lost the supply to a healthy inverter leg of another motor. The concept is illustrated in Fig. 1 for a two-motor drive, where, after open-circuiting of the phase *c* of the second motor, the supply for this phase is connected in parallel to phase *c* supply of the first motor.

The resulting inverter topology in Fig. 1 is a five-leg inverter supplied two-motor drive, which has been considered extensively in the past as one of the reduced-switch-count topologies for multi-motor drive systems [1-3]. The five-leg configuration provides a similar fault-tolerant property as the addition of a redundant inverter leg, studied in [4], except that the control is here more involved due to the sharing of an inverter leg between the machines. It is important to emphasize that all phases are energized here after the fault, in contrast to the configuration in [5], and hence a higher and smoother torque can be obtained.

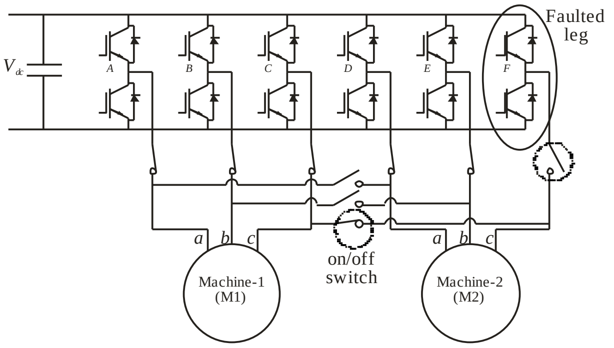

Fig. 1. Reconfiguration of the electrical connections of the two-motor system through appropriate on/off switches after a fault in one inverter leg.

In post-fault operation shared inverter leg topology of Fig. 1 leads to a limited dc-bus voltage availability, as well as the potentially (depending on the loading) higher current flow in the shared inverter leg [3]. Full utilization of the available dc-bus voltage in an *m*-motor drive supplied by a (2*m*+1)-leg VSI is possible using the suitable PWM techniques developed in [2-3]. Since the dc-bus voltage is set to the value that corresponds to a single-motor drive, even with the full dc-bus voltage utilization, there is a limit on the achievable operating speeds, which in simple terms means that the sum of the frequencies of any two machines cannot exceed rated supply frequency.

MPC has been introduced into the drives area in the last decade and the most frequent form is the FCS-MPC. Using FCS-MPC, various machine control schemes have been studied, including flux and torque [6-7], and speed [8] control. FCS-MPC has been also recently applied in the two-motor drive system supplied by a five-leg inverter [9], where synchronous current control has been investigated.

In this work, which builds on [10], flux and torque control based on FCS-MPC is addressed. The simultaneous consideration of the two motors and the five-leg inverter as a single system by the FCS-MPC gives rise to a new control approach, which leads to two significant improvements over [2-3, 9]: (i) extension of the operating speed ranges; (ii) maximum utilization of the dc-bus voltage for the torque production at all times. Through a proper design of the cost function (and the associated prediction part), three possible modes of operation are investigated. The first mode is fully

---

Manuscript received December 3, 2013; revised February 26, 2014; accepted March 30, 2014.

C.S. Lim was with the University of Malaya, UMPEDAC Research Center, Kuala Lumpur, Malaysia and with Liverpool John Moores University, School of Engineering, Technology and Maritime Operations, Liverpool L3 3AF, U.K. (e-mail: limcheeshen@gmail.com).

E. Levi and M. Jones are with the School of Engineering, Technology and Maritime Operations, Liverpool John Moores University, Liverpool L3 3AF, U.K. (e-mails: e.levi@ljmu.ac.uk and m.jones2@ljmu.ac.uk).

N.A. Rahim and W.P. Hew are with the UMPEDAC Research Centre, Wisma R&D, University of Malaya, 59990, Kuala Lumpur, Malaysia (e-mails: nasrudind@um.edu.my and wphew@um.edu.my).

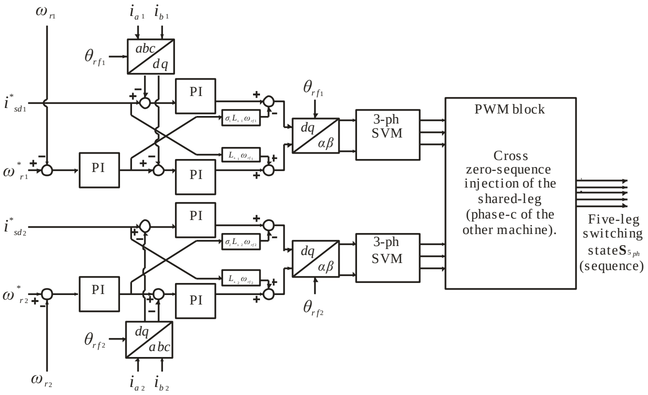

Fig. 2. Block diagram of the conventional PI-based two-motor field-oriented control (FOC) scheme [8] (SVM – space vector modulation).

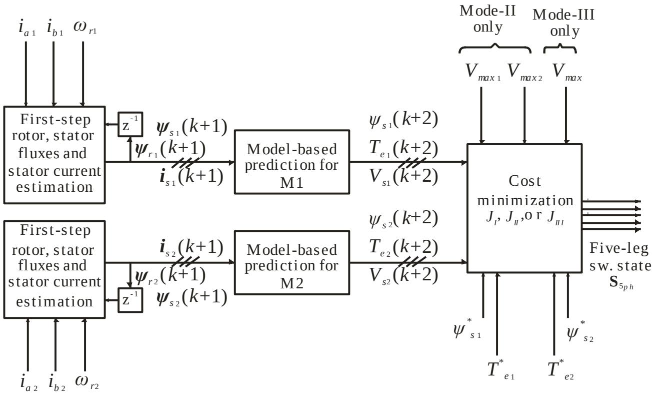

Fig. 3. Block diagram of the FCS-MPC algorithms.

equivalent to the conventional PWM scheme with arbitrary dc-bus voltage allocation [2] and hence full dc-bus voltage utilization. The second mode is very similar to the PWM scheme with the pre-allocated dc-bus voltage [1], which does not provide full dc-bus voltage utilization; however, it yields extended speed ranges. The third mode appears to be the best since it not only provides full dc-bus voltage utilization, but also naturally extends the range of possible operating speeds way beyond those available in the first mode. It is shown that this is enabled by the unique way in which MPC handles constraints and tracking errors.

The control principles, introduced in [10], are at first revisited. Simulation proof of concept is given in [10] and a full set of experimental results is presented here instead. Finally, a comparison of the performance with respect to the standard field-oriented control is also included and superiority of the FCS-MPC approach is thus confirmed.

II. FIELD-ORIENTED CONTROL SCHEME

Throughtout the paper, without any loss of generality, it is assumed that due to the fault in phase *c* of the second motor, phase-*c* of each machine is connected to the leg-*C* of the inverter, as shown in Fig. 1, in post-fault operation.

As noted, the performance of the developed FCS-MPC flux and torque control schemes will be compared to the field-oriented control, which is for the two-motor drive illustrated in Fig. 2. Two main PWM methods were developed in the past. The first one pre-allocates half of the dc-bus voltage to each machine [1], regardless of the operating conditions of the other machine, so that only operation up to the half of the rated speed is possible in the linear PWM region. The other, identified in the PWM block of Fig. 2, provides arbitrary allocation of the dc-bus voltage to the machines [2,3], so that when one machine runs at low speed, more voltage is available for the other machine and the dc-bus voltage can always be fully utilized. However, simultaneous voltage demands of the two machines still cannot exceed the limit imposed by the dc-bus voltage, meaning that operation in the linear PWM region is possible as long as, in layman's terms, sum of the speeds of the two machines does not exceed the rated speed of the machine.

III. PREDICTIVE MODEL

A five-leg inverter has 32 switching states. A complete evaluation of this control input set would require 32 sets of variable and cost function computations. Owing to the presence of redundancy, the computational effort can be reduced by using seven feasible switching states per motor without affecting the control performance [9], and such an approach is adopted here. The schematic block diagram of the control system is shown in Fig. 3. Stator flux and torque control based on FCS-MPC is explained next, by referring to one induction machine; the same applies to the other one. Since only the stator currents and the rotor speed (position) are the measured variables, while all the other quantities are either estimated or predicted, estimated/predicted variables are not identified with a special symbol in the notation further on.

Stator flux can be predicted using the rotor flux model,

$$\boldsymbol{\psi}_s = \frac{L_m}{L_r}\boldsymbol{\psi}_r + \sigma L_s \boldsymbol{i}_s \tag{1}$$

or by using the stator voltage model in integral form:

$$\frac{d\boldsymbol{\psi}_s}{dt} = -R_s\boldsymbol{i}_s + \boldsymbol{v}_s \;\;\Rightarrow\;\; \boldsymbol{\psi}_s = \int(-R_s\boldsymbol{i}_s + \boldsymbol{v}_s)\cdot dt \tag{2}$$

Here $\boldsymbol{\psi}_s = \psi_{s\alpha} + j\psi_{s\beta}$ represents the stator flux vector in the stationary reference frame, which is used further on in the form $[\psi_{s\alpha}\ \psi_{s\beta}]^T$. The same notation applies to $\boldsymbol{i}_s$, $\boldsymbol{v}_s$, and $\boldsymbol{\psi}_r$. L_m and L_r (L_s) represent the mutual and rotor (stator) inductances, while σ and R_s (R_r) denote the leakage factor and the stator (rotor) resistance. In general, (1) is of higher accuracy than (2), since the parasitic phenomena lead to discrepancy between the reconstructed voltages and the realized voltages in the actual inverter's output. Integral of this error in (2) may lead to erroneous predictions. However, (1) is more complex regarding implementation as the prediction of the rotor flux components is also required in the FCS-MPC's iterative prediction stage [9], although only stator flux is needed during optimization.

In the actual FCS-MPC implementation, two-step-ahead prediction is always used to overcome the high computational delay. The first step prediction in essence extrapolates the measured variables to a sampling period ahead, and the values then become the initial conditions for the predictive algorithm ([7] and references therein). To achieve a balance between higher accuracy and simplicity, the first-step stator flux vector is predicted using (1), requiring the estimation of the rotor flux vector in the control algorithm, while (2) is used in the iterative prediction stage (second step). It must be emphasized that the rotor flux is estimated in an open-loop manner and there is no corrective feedback available. This means that the accuracy of the estimation depends heavily on the knowledge of rotor parameters and how precise the discrete-time estimator is. In this study, the discrete-time model, used in the first-step prediction, provides correct estimation of the rotor flux vector, as discussed in the forthcoming subsection. Estimating the stationary-axis rotor flux space vector using low-order discretization technique, such as for example Euler method, would lead to deviation of the estimated value from the actual one [6].

A. The First-Step Prediction

The continuous-time state-space (SS) model of a three-phase machine with stator current and rotor flux components as the state-space variables is:

$$\dot{\mathbf{x}}(t) = \mathbf{A}_t\mathbf{x}(t) + \mathbf{B}_t\mathbf{u}(t) \tag{3}$$

where $\mathbf{x} = [\boldsymbol{i}_s \quad \boldsymbol{\psi}_r]^T$, $\mathbf{u} = [\boldsymbol{v}_s]$. Note that the state matrix $\mathbf{A}_t$ is time-variant in nature, while the input matrix $\mathbf{B}_t$ is not. Model (3) is written in discrete-time domain at time $t=kT$ as

$$\mathbf{x}(k+1) = \mathbf{\Phi}_k\mathbf{x}(k) + \mathbf{\Gamma}_k\mathbf{u}(k) \tag{4}$$

By resolving $\mathbf{A}_t$ into time-invariant and time-variant parts, and by using Cayley-Hamilton theorem to obtain the exp($\mathbf{A}_tT$), required for determination of the discrete-time coefficients $\mathbf{\Phi}_k$ and $\mathbf{\Gamma}_k$ (defined in the Appendix) in (4) [6], a discrete-time rotor flux estimator is obtained

$$\boldsymbol{\psi}_r(k+1) = \mathbf{\Phi}_{k,row3,4}\begin{bmatrix}\boldsymbol{i}_s(k)\\ \boldsymbol{\psi}_r(k)\end{bmatrix} + \mathbf{\Gamma}_{k,row3,4}[\boldsymbol{v}_s(k)] \tag{5}$$

On the other hand, the first-step stator current vector is also predicted using the model (4), as:

$$\boldsymbol{i}_s(k+1) = \mathbf{\Phi}_{k,row1,2}\begin{bmatrix}\boldsymbol{i}_s(k)\\ \boldsymbol{\psi}_r(k)\end{bmatrix} + \mathbf{\Gamma}_{k,row1,2}[\boldsymbol{v}_s(k)] \tag{6}$$

The first-step stator flux is then predicted using (1), as

$$\boldsymbol{\psi}_s(k+1) = \frac{L_m}{L_r}\boldsymbol{\psi}_r(k+1) + \sigma L_s\boldsymbol{i}_s(k+1) \tag{7}$$

B. The Second-Step Prediction

Three-phase inverter model gives the stator voltage space vectors as:

$$\boldsymbol{v}_s(k+1) = V_{dc}\mathbf{C}(\mathbf{VS}(k+1)) \tag{8}$$

where V_{dc} is the dc-bus voltage, $\mathbf{S} = [s_a \quad s_b \quad s_c]^T$, s_i={0,1}, and i = a,b,c represents phases a, b, and c. $\mathbf{C}$ and $\mathbf{V}$ are the decoupling and leg-to-phase voltage transformations

$$\mathbf{C} = \frac{2}{3}\begin{bmatrix}1 & \cos(2\pi/3) & \cos(4\pi/3)\\ 0 & \sin(2\pi/3) & \sin(4\pi/3)\end{bmatrix} \tag{9a}$$

$$\mathbf{V} = \frac{1}{3}\begin{bmatrix}2 & -1 & -1\\ -1 & 2 & -1\\ -1 & -1 & 2\end{bmatrix} \tag{9b}$$

The switching states from the two three-phase systems will be eventually combined in the cost function to form the five-leg switching state, discussed in Section IV. The switching states $[0\ 0\ 0\ 0\ 0]^T$ and $[1\ 1\ 1\ 1\ 1]^T$ are redundant; hence, when a zero switching state is required, the one that gives fewer switching commutations is selected and applied.

Predictions in the second step are required for the open-loop optimization algorithm to find the best switching state among the discrete switching states. The first-order discretized (forward-Euler) models of $\boldsymbol{i}_s$ (based on (3)) and $\boldsymbol{\psi}_s$ (based on (2)) are used to predict the future stator current and stator flux components at horizon time (k+2)T:

$$\boldsymbol{i}_s(k+2) = \begin{bmatrix}1 - T(\frac{1}{\sigma T_s} + \frac{1-\sigma}{\sigma T_r}) & 0\\ 0 & 1 - T(\frac{1}{\sigma T_s} + \frac{1-\sigma}{\sigma T_r})\end{bmatrix}\boldsymbol{i}_s(k+1) + \begin{bmatrix}T(\frac{1-\sigma}{\sigma L_m T_r}) & T\frac{(1-\sigma)\omega_{re,k}}{\sigma L_m}\\ -T\frac{(1-\sigma)\omega_{re,k}}{\sigma L_m} & T(\frac{1-\sigma}{\sigma L_m T_r})\end{bmatrix}\boldsymbol{\psi}_r(k+1) + \begin{bmatrix}\frac{T}{\sigma L_s} & 0\\ 0 & \frac{T}{\sigma L_s}\end{bmatrix}\boldsymbol{v}_s(k+1) \tag{10}$$

$$\boldsymbol{\psi}_s(k+2) = \boldsymbol{\psi}_s(k+1) - R_sT\boldsymbol{i}_s(k+1) + T\boldsymbol{v}_s(k+1) \tag{11}$$

Stator flux magnitude and electromagnetic torque are predicted next (vector dot and cross products are used and P is the number of pole pairs),

$$\begin{aligned}\psi_s(k+2) &= \sqrt{\boldsymbol{\psi}_s(k+2)\cdot\boldsymbol{\psi}_s(k+2)}\\ T_e(k+2) &= (3/2)P|\boldsymbol{\psi}_s(k+2)\times\boldsymbol{i}_s(k+2)|.\end{aligned} \tag{12}$$

IV. COST FUNCTION DESIGN

A. Basic Considerations

The stator flux and electromagnetic torque of Machine-1 are to be tracked, requiring the cost component j_{M1}:

$$j_{M1} = \frac{1}{T_{e1,nom}^2}(T_{e1}^*(k+2) - T_{e1}(k+2))^2 + \frac{\lambda_{f1}}{\psi_{s1,nom}^2}(\psi_{s1}^*(k+2) - \psi_{s1}(k+2))^2 \tag{13}$$

Symbol λ stands for a weighting factor, while *nom* in index stands for nominal (rated) value. Note that the weighting for T_{e1} error is 1 by default. On the other hand, j_{M2} is used for the control of Machine-2:

$$j_{M2} = \frac{\lambda_{T2}}{T_{e2,nom}^2}(T_{e2}^*(k+2) - T_{e2}(k+2))^2 + \frac{\lambda_{f2}}{\psi_{s2,nom}^2}(\psi_{s2}^*(k+2) - \psi_{s2}(k+2))^2 \tag{14}$$

For over-current protection, the instantaneous peak phase currents of both machines must be smaller than the respective maximum allowed values ($I_{\max}$), giving j_i:

$$\begin{aligned}j_i = \lambda_i[((i_{s\alpha,1}^2(k+2) + i_{s\beta,1}^2(k+2)) > I_{1,\max}^2)\ \mathrm{OR}\\ ((i_{s\alpha,2}^2(k+2) + i_{s\beta,2}^2(k+2)) > I_{2,\max}^2)]\end{aligned} \tag{15}$$

j_i/λ_i is equal to 1 when any of the over-current conditions is active and λ_i should be set to a very high value.

B. Shared-Leg and Voltage Considerations

The shared-leg topology is not considered in the model prediction stage; it must be considered now in the cost function to eliminate the infeasible combinations of the individual three-phase switching states. The two sets of switching states must have the same phase-c state. Thus, their difference forms the cost component j_{leg}:

$$j_{leg} = \lambda_{leg}|s_{c,1} - s_{c,2}| \tag{16}$$

$|s_{c,1}$-$s_{c,2}|$ is equal to 1 when there is a difference between the two phase-c states, and λ_{leg} is set to a very large value to signify the hard constraint.

The total fundamental voltage demand by the two machines must not exceed the maximum voltage available from the dc bus. The handling of this constraint in the existing PWM based control methods essentially relies on limiting the operating speed ranges of the two machines. Here, the voltage constraint will be included into the FCS-MPC algorithm. This requires the fundamental voltage components. With PWM, the instantaneous amplitude and phase of the fundamental output voltage are, neglecting parasitic effects, equal to the reference values (e.g., modulating signal amplitude and phase in the carrier-based PWM or magnitude and phase of the reference space vector in space vector PWM). In the case of the generic FCS-MPC, only a single actual voltage vector (VV) is impressed in a switching period; thus finding the instantaneous voltage amplitude from the reference voltage is not possible. Hence, the fundamental voltage amplitude is approximated as follows. The voltage consideration is only active when both machines operate at relatively high speeds, when the resistive voltage drop term in the stator voltage equation (2) can be neglected, giving:

$$V_s \approx \left|\frac{d\boldsymbol{\psi}_s}{dt}\right| = |\omega_{se}||\boldsymbol{\psi}_s| = |\omega_{se}|\psi_s \tag{17}$$

or, in discrete-time domain,

$$V_s(k+2) = |\omega_{se}(k+2)|\psi_s(k+2) \tag{18}$$

Also, owing to the steady state assumption, the stator flux electrical speed remains constant from horizon time $(k+1)T$ to $(k+2)T$ and is equal to the speed of the rotor flux vector at $(k+1)T$, i.e. in the first-step prediction, approximated using:

$$\theta_{re}(k+1) = \tan^{-1}\frac{\psi_{r\beta}(k+1)}{\psi_{r\alpha}(k+1)}$$

$$\omega_{se}(k+1) = \omega_{re}(k+1) = \frac{\Delta\theta_{re}}{\Delta t} = \frac{\theta_{re}(k+1) - \theta_{re}(k)}{T} \tag{19}$$

The predicted stator voltage amplitude $V_s(k+2)$ of (18) is further included in the cost function for dc-bus voltage consideration.

C. Modes of Operation

Three cost function designs are introduced, which correspond to three modes of operation. Mode-I is a mode that does not consider voltage constraint in the cost function. The cost function J_I is defined simply as:

$$J_I = j_{M1} + j_{M2} + j_{leg} + j_i \tag{20}$$

Mode-I is expected to be equivalent to the arbitrary dc-bus allocation scheme with PWM [2]. When the total voltage demand exceeds what the dc-bus can give, voltage constraint will be violated, over-modulation region will be entered, and large torque oscillations will appear. The second mode of operation, Mode-II, is obtained by pre-allocating part of the dc-bus voltage to each machine. The associated J_{II} is

$$J_{II} = j_{M1} + j_{M2} + j_{leg} + j_i + j_{V1} + j_{V2} \tag{21}$$

where

$$j_{V1} = \frac{\lambda_{V1}}{V_{\max}^2}(V_{s1}(k+2) > V_{\max1})(V_{\max1} - V_{s1}(k+2))^2$$

$$j_{V2} = \frac{\lambda_{V2}}{V_{\max}^2}(V_{s2}(k+2) > V_{\max2})(V_{\max2} - V_{s2}(k+2))^2$$

$$V_{\max1} = 0.5V_{\max}$$

$$V_{\max2} = V_{\max} - V_{\max1}$$

Equal, 50% dc-bus voltage allocation is assumed here. Hence the resulting operation is expected to be very similar to the PWM scheme of [1]. V_{max1} and V_{max2} are the maximum ac equivalent voltages allocated to Machine-1 and Machine-2, respectively. V_{max} is the maximum ac-equivalent voltage value available, determined by the dc-bus voltage and it will be discussed later.

Finally, Mode-III is introduced. Instead of pre-allocating the voltage to each machine, the voltage constraint consideration is imposed on the sum of the two voltage demands. The associated cost function J_{III} is now:

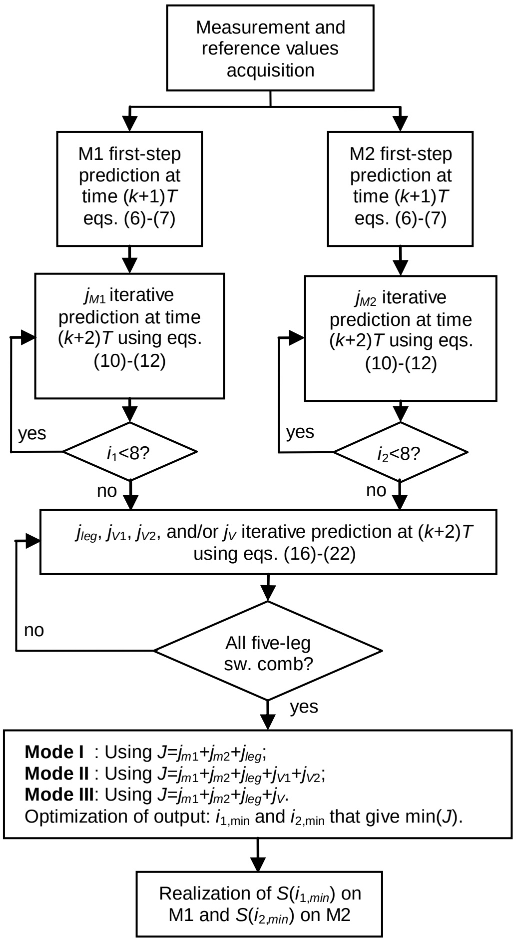

Fig. 4. A general algorithm flow chart of Mode-I, Mode-II, and Mode-III. (Symbol *i* stands for the state number).

$$J_{III} = j_{M1} + j_{M2} + j_{leg} + j_i + j_V \tag{22}$$

where

$$j_V = \frac{\lambda_V}{V_{\max}^2}(V_{sum}(k+2) > V_{\max})(V_{\max} - V_{sum}(k+2))^2$$

$$V_{sum}(k+2) = V_{s1}(k+2) + V_{s2}(k+2)$$

This mode keeps the arbitrary dc-bus voltage allocation to both machines, as in Mode-I, while respecting the constraint of the limited total dc-bus voltage.

The flow chart, which represents all three FCS-MPC schemes, is given in Fig. 4.

D. Selection of V_{max}

Voltage limit is not simply a hard constraint but is regarded as a soft constraint here, requiring a proper setting of weighting factors λ_{V1}, λ_{V2}, and λ_V, and is significantly different from over-current (15) and leg-*C* state (16) hard constraints. V_{max} is set here to $0.5V_{dc}$ in Mode-II and Mode-III operation. It has to be noted that, in the initial study in [10], the value was set to V_{max}=$0.577V_{dc}$, which corresponds to the limit of the linear PWM region with zero-sequence injection. It was concluded (and will be shown shortly) that the limit of $0.5V_{dc}$ (which corresponds to the maximum modulation index in the linear PWM region without zero-sequence injection) gives a better overall performance especially during transients, when compared to $0.577V_{dc}$.

This suggests that the level of dc-bus voltage utilization in the direct control of inverter switching states, as in FCS-

MPC, is different in nature compared to the PWM (exact formulation of the maximum sinusoidal voltage obtainable with the FCS-MPC is outside the scope of this paper). The justification for taking V_{max} as $0.5V_{dc}$ is further supported by the following practical considerations: (i) dead-time effect lowers the maximum achievable fundamental voltage; (ii) predicted $V_{s1,2}$ may be different from the actual machines' fundamental voltages due to the neglected resistive voltage drop in (18); and, (iii) as evidenced later, the predicted $V_{s1,2}$ and/or V_{sum} tend to remain slightly higher than the imposed limits $V_{max1,2}$ and/or V_{max} in steady state with active voltage constraint, due to their soft-constraint nature.

It should be emphasized here that the choice of V_{max} is always such that the inverter remains at all times in the linear modulation region, since entering the over-modulation or even six-step region would drastically increase the torque (and current) ripple.

V. EXPERIMENTAL RESULTS

The test rig, used in the subsequent experimental investigation, consists of two 2.2kW three-phase four-pole induction motors and a five-leg two-level inverter (Fig. 5) Microcontroller TMS320F28335 is used. The dc-bus voltage is provided by a dc power supply and is set to 450V due to hardware limitations. Consequently, the stator flux magnitude references, ψ_{s1}^* and ψ_{s2}^*, for the two machines during drive initialization are set to 0.73 Wb, which is commensurate with the dc-bus voltage and gives approximately 3/4 of the rated motor phase voltage (240V) at rated (50Hz) frequency. Other machine and FCS-MPC parameters are listed in Table I. M1 and M2 are operated in closed-loop speed control mode, with the same amount of purely inertial load on the shaft. The FCS-MPC algorithm is executed at 10 kHz sampling frequency but all data are captured at 5 kHz sampling frequency due to the limited external memory for data logging for long time duration. The weighting factors are set as follows: $\lambda_{f1} = \lambda_{f2} = 15$; $\lambda_{T2} = 1$; $\lambda_{V1} = \lambda_{V2} = \lambda_V = 150$, with some tuning taking place experimentally. It should be noted that the maximum current limit (i.e. cost term j_i in (15)) is not imposed at all in order to reduce the computation burden.

TABLE I: PARAMETERS IN THE EXPERIMENTAL SETUP

Parameter	Value	
Sampling period, T	100µs	
Dead time	4 µs	
	Machine-1	**Machine-2**
Stator phase resistance R_{s1}	2.43 Ω	2.43 Ω
Rotor phase resistance R_{r1}	1.59 Ω	1.69 Ω
Stator leakage inductance L_{ls1}	11.9 mH	12.3 mH
Rotor leakage inductance L_{lr1}	11.9 mH	12.3 mH
Mutual inductance, L_{m1}	296 mH	308 mH
Rated voltage (line-line, rms)	415 V	
Rated frequency	50 Hz	
Rated current (rms)	4.5 A	
Rated torque	14.6 Nm	
Rotor inertia	0.0103 kgm^2	
Rated speed	1440 rpm	
Number of pole pairs, P	2	

A. Operation at Low Speed/Angular Frequency Sum

The settings of V_{dc}, ψ_{s1}^* and ψ_{s2}^* in the experiments allow both motors to operate properly provided the sum of steady-state stator angular frequencies (i.e. motor electrical angular speeds, due to the no-load conditions) is up to 100π rad/s. Fig. 6 shows Mode-I operation with inactive voltage constraint in which M1 speed reference (ω_{r1}^*) is stepped from zero to 60 rad/s at time 0.2s and then back to zero at 2.2s, while M2 speed command (ω_{r2}^*) remains at 70 rad/s. It can be seen that the FCS-MPC successfully controls the flux and torque of each machine.

Fig. 7 shows the corresponding leg-C current and the predicted V_{s1}, V_{s2}, V_{sum} for the same conditions as in Fig. 6 (but recorded separately, due to the limited number of data-

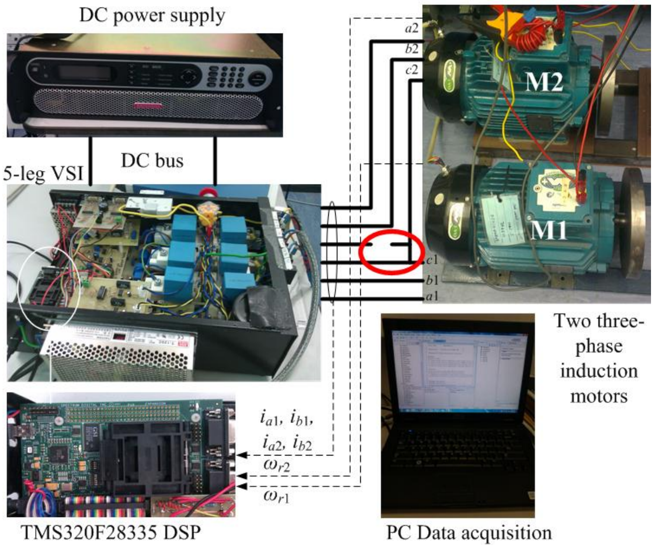

Fig. 5. Experimental test rig.

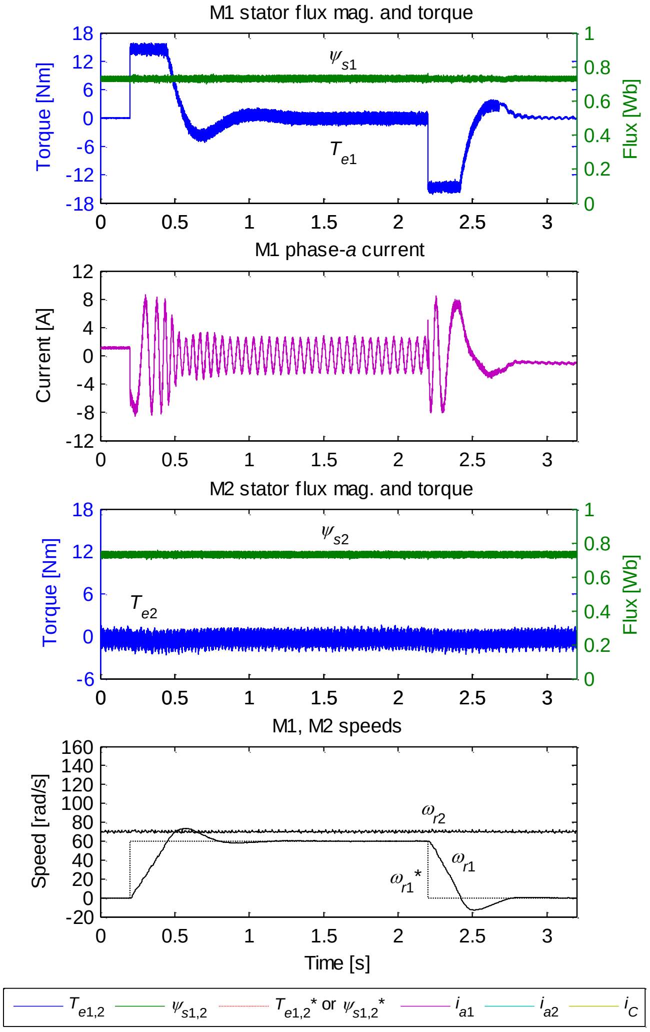

Fig. 6. Experimental results showing Mode-I operation with inactive voltage constraint.

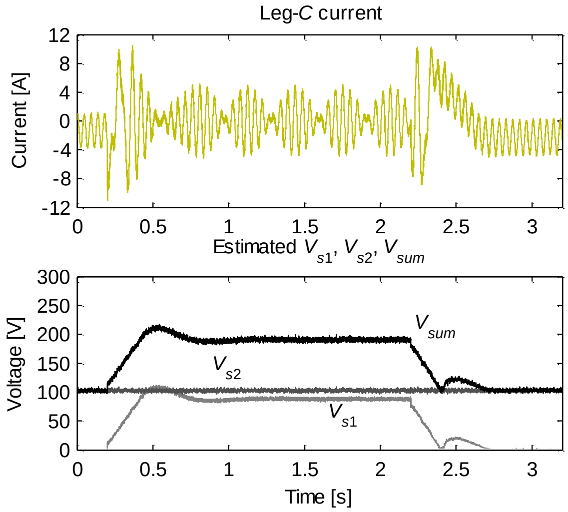

Fig. 7. Inverter leg-*C* current, and predicted fundamental peak voltages for Mode-I operation. Conditions as in Fig. 6, a separate recording.

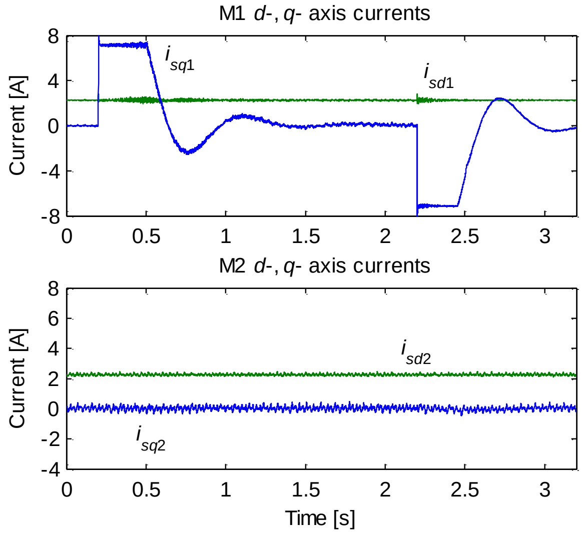

Fig. 8. Stator *d*-axis and *q*-axis currents in both machines with the conventional two-motor FOC scheme for the same test conditions as in Figs. 6 and 7.

logging channels in the DSP). The leg-*C* current trace contains two fundamental frequency components, each belonging to one machine [2]. The predicted fundamental voltage amplitude sum V_{sum} has a steady-state value close to 200V during the interval from 1.0s to 2.2s.

Next, Fig. 8 shows the stator *d*-axis and *q*-axis currents of both machines in a test with the existing two-motor field-oriented control scheme of Fig. 2. M1 speed reference is stepped from zero to 60 rad/s at 0.2s and then back to zero at 2.2s, while M2 is kept at 70 rad/s. Since the speed sum is 130 rad/s, i.e. less than the approximate threshold of 50π rad/s (mechanical) for linear inverter operation, the machine currents are well controlled.

B. Operation at High Speed/Angular Frequency Sum without Voltage Limit Consideration

Mode-I operation with the activation of the voltage constraint but without any control intervention is shown in Fig. 9, where reference speeds are set to 130rad/s and 70rad/s for M1 and M2, respectively. It can be seen from the flux and torque traces in Fig. 9 that the voltage constraint is entered around *t*=0.66s, when the motor angular speed sum exceeds approximately 50π rad/s. Although the motor speeds can still be controlled to their reference values due to closed speed loops, excessive fluctuations appear in the

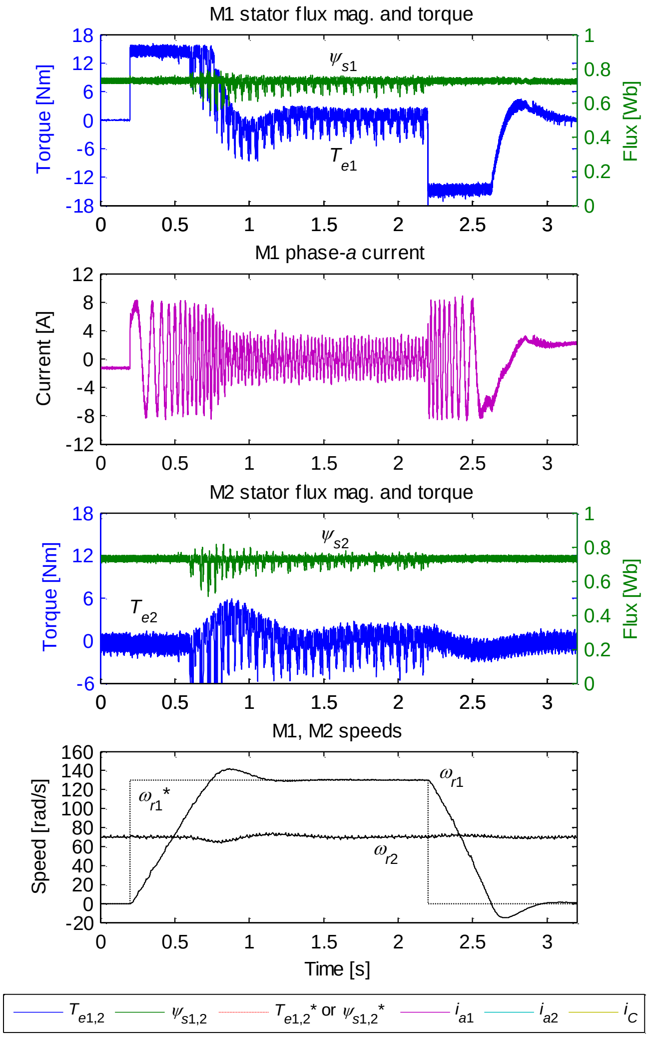

Fig. 9. Experimental results showing Mode-I operation with the activation of the voltage constraint.

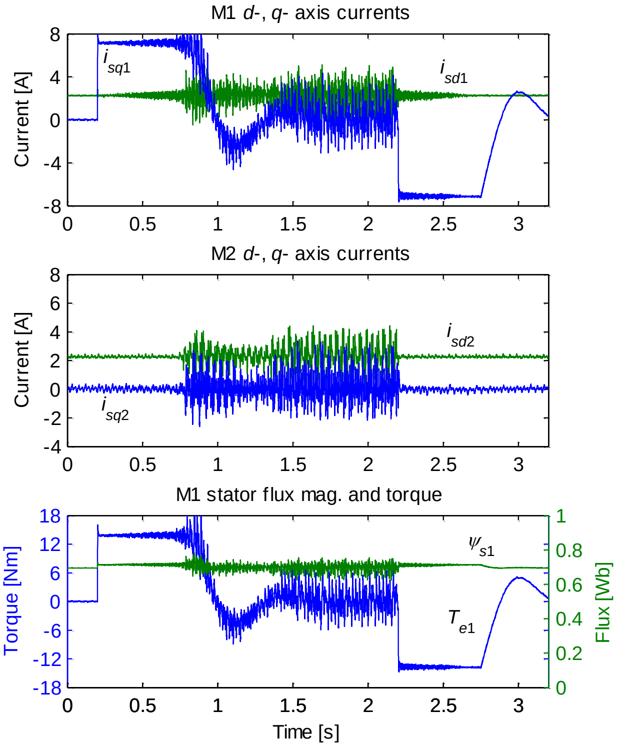

Fig. 10. Stator *d*-axis and *q*-axis currents in both machines for the conventional two-motor FOC scheme, for the same test as in Fig. 9. The motor speeds sum to 200 rad/s.

predicted flux and torque of both machines. This is undesirable, as the machine currents become highly distorted (Fig. 9). The same test has been also conducted with the FOC scheme and the results are shown in Fig. 10. Large current fluctuations are evident in the synchronous *d-q* currents when the sum of the speeds exceeds 50π rad/s.

With the known machine parameters, *d-q* current data have been post-processed to obtain the machine stator flux and torque estimates and the traces (for M1 only) are also plotted in Fig. 10. The torque fluctuation is even worse than the one in Fig. 9.

C. Operation at High Speed/Angular Frequency Sum with Voltage Limit Consideration

Mode-II operation (with $V_{max1}= V_{max2}= 0.5V_{max}$, i.e. equal dc-bus voltage allocation) with the activation of voltage constraint is examined using the same reference speed settings as for Fig. 9 and the results are given in Figs. 11 and 12. Flux ψ_{s1} starts to reduce at about 0.485s, i.e. the instant when M1 speed reaches ≈70 rad/s. This is also the instant when V_{s1} reaches the imposed limit of V_{max1} (Fig. 12). For a short subsequent time interval the FCS-MPC controller attempts to keep T_{e1} constant at the imposed rated torque limit, while the motor speed continues to increase and ψ_{s1} continues to decrease. However, a careful inspection of T_{e1} and ψ_{s1} traces reveals that a slight drop in T_{e1} takes place from 0.6s to 0.7s, and this will be explained later. At steady-state speed of 130rad/s (from 1.5s to 2.2s) ψ_{s1} remains at ≈0.46Wb (but $\psi_{s1}^*= 0.73$Wb). This is intepreted from the control perspective as a tracking error (i.e. offset), while it is seen from the machine's operational perspective as a field weakening operation. Different from the PI-based control method, there is no need to reduce ψ_{s1}^*, thanks to MPC characteristic that respects the imposed voltage limits. Of course, for the whole control concept to work well a proper design of the model, cost function and weighing factors is required.

After 2.2s, ω_{r1}^* is stepped back from 130 rad/s to zero (Fig. 11). As the motor speed decreases, ψ_{s1} is gradually restored towards ψ_{s1}^* while V_{s1} is kept approximately constant. The stator flux tracking offset/error gets zeroed when M1 speed falls below ≈86 rad/s at t=2.35s. There is a difference between this value and the speed threshold during acceleration (≈70 rad/s), which is due to the opposite sign of the angular slip frequency during acceleration and deceleration.

The results in Figs. 11-12 show the unique control capability of MPC, which allows the presence of stator flux tracking offsets whenever the voltage limit is entered. In the conventional schemes, a change of flux magnitude reference is required for field weakening [11]. The unique mode of operation, enabled by the FCS-MPC in Mode-II (and Mode-III as well, as discussed shortly) demonstrates so-called base-speed field weakening (BSFW), i.e. occurrence of field weakening in the base speed region that overcomes the flux/torque fluctuations caused by limited voltage of this drive topology.

Next, Mode-III operation with the activation of voltage constraint is illustrated in Figs. 13 and 14. When M1 speed reaches ≈78 rad/s at about 0.53s, both machines' stator flux magnitudes start to reduce. The field weakening operation is only initiated when the total dc-bus voltage is used up (as shown by the V_{sum} trace in Fig. 14). Similarly, as M1 attains higher speeds, the controller maintains T_{e1} (and T_{e2}) while reducing both ψ_{s1} and ψ_{s2}. In the subsequent steady state (1.5s to 2.2s) both ψ_{s1} and ψ_{s2} settle down at 0.54Wb and 0.63Wb respectively ($\psi_{s1}^*=\psi_{s2}^*=0.73$Wb). This is similar to Mode-II in a sense that the field weakening mechanism does not require any *a priori* change of the ψ_{s1}^* and ψ_{s2}^* values.

Similar to Mode-II, the amount of field weakening reduces and eventually deactivation takes place upon the decrease of M1 speed ω_{r1}, after 2.2s. Both ψ_{s1} and ψ_{s2}

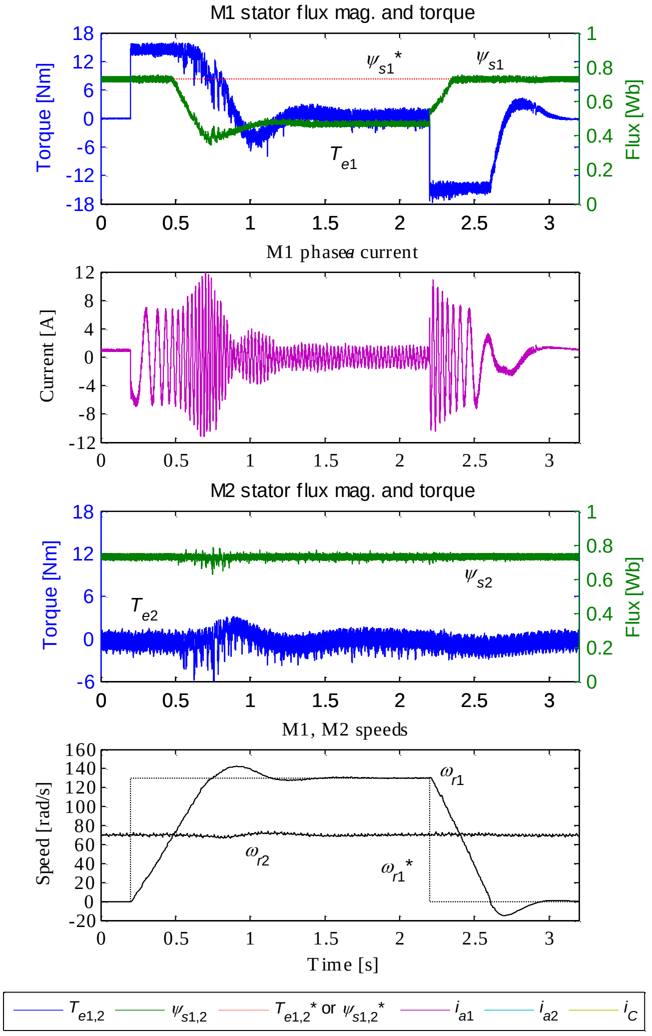

Fig. 11. Experimental results showing Mode-II operation with the activation of the voltage constraint.

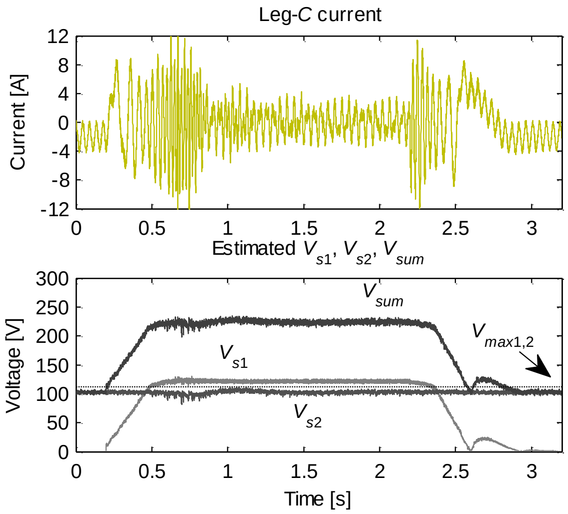

Fig. 12. Inverter leg-*C* current and predicted fundamental voltage amplitudes for Mode-II operation. Conditions as in Fig. 11.

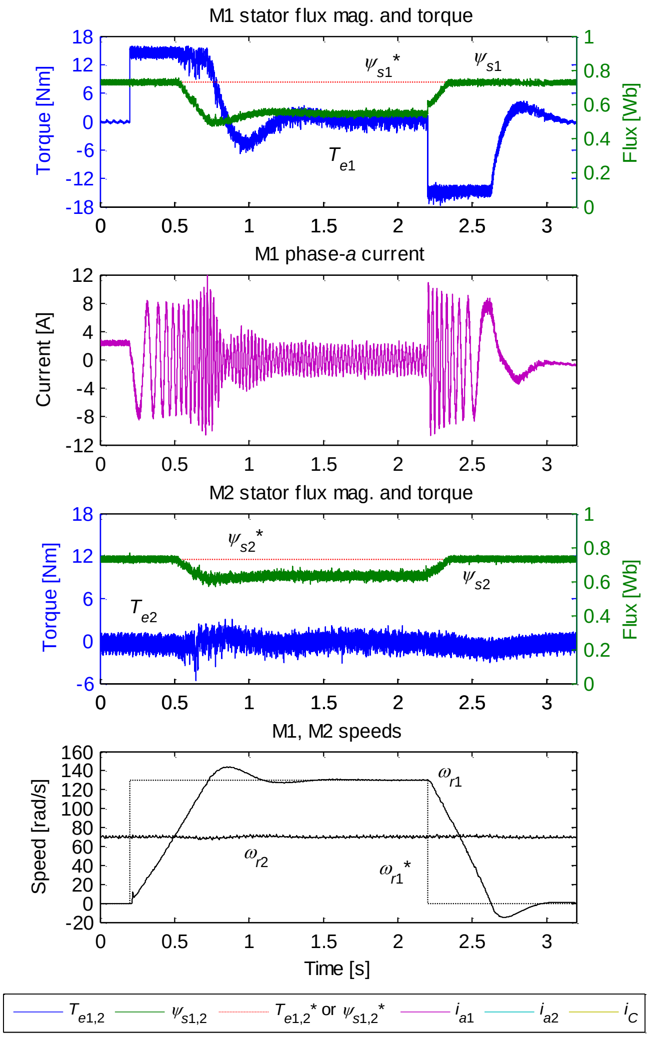

Fig. 13. Experimental results showing Mode-III operation with the activation of the voltage constraint.

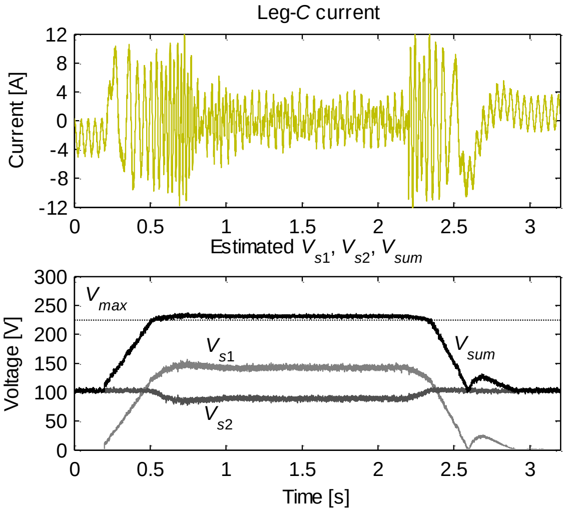

Fig. 14. Inverter leg-C current and predicted fundamental voltage amplitudes for Mode-III operation. Conditions as in Fig. 12.

return back to ψ_{s1}^* and ψ_{s2}^* gradually, before V_{sum} gets reduced below the imposed limit V_{max} when M1 speed falls below ≈94 rad/s. This is again different from the threshold value during acceleration, for the same reason as discussed in conjunction with Mode-II. The comparison of current traces also shows that, during non-zero torque production, the machine currents are higher in Mode-II than in Mode-III, which is expected since Mode-II caused deeper field weakening than Mode-III.

VI. DISCUSSION

A. Comparison with the PI based FOC scheme

For a complete evaluation and comparison of the control schemes, the conventional FOC scheme for the two-motor drive needs to be modified. One solution is shown in Fig. 15. Each machine's d-axis current reference will be decreased once the machine's speed exceeds the preset speed threshold. The threshold speeds are set to 25π rad/s, giving an equal allocation of the dc-bus voltage to machines.

The experimental results, for the same conditions as in Figs. 11 and 13, are shown in Fig. 16. After the preset speed threshold is exceeded, M1's d-axis current i_{sd1} reduces from 1.6√2A to approximately 0.98√2 A after about 1.2s. Note that M1's torque has been reduced in the interval from 0.5s to 1s and 2.2s to 2.7s, and the machine's operation is similar to the results in Fig. 11. Hence this FOC scheme serves as the counterpart of FCS-MPC's Mode-II scheme since they have the same individual machine's field weakening characteristics.

A field-oriented control scheme, which would be a counterpart of the FCS-MPC Mode-III scheme, would require simultaneous field weakening of both machines whenever the speed sum exceeds a preset value. Thus each machine's control algorithm would have to consider the

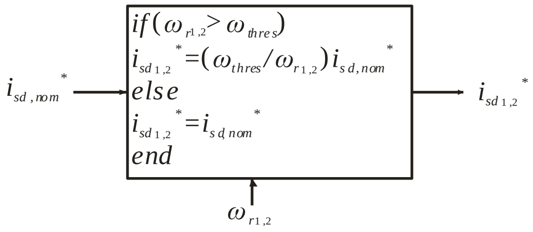

Fig. 15. Adjustment of d-axis current reference in the conventional FOC scheme. ω_{thres} and $i_{sd,nom}$ are the field weakening threshold speed (25πrad/s, signifying equal dc-bus voltage allocation) and the chosen nominal d-axis current (1.6√2 A).

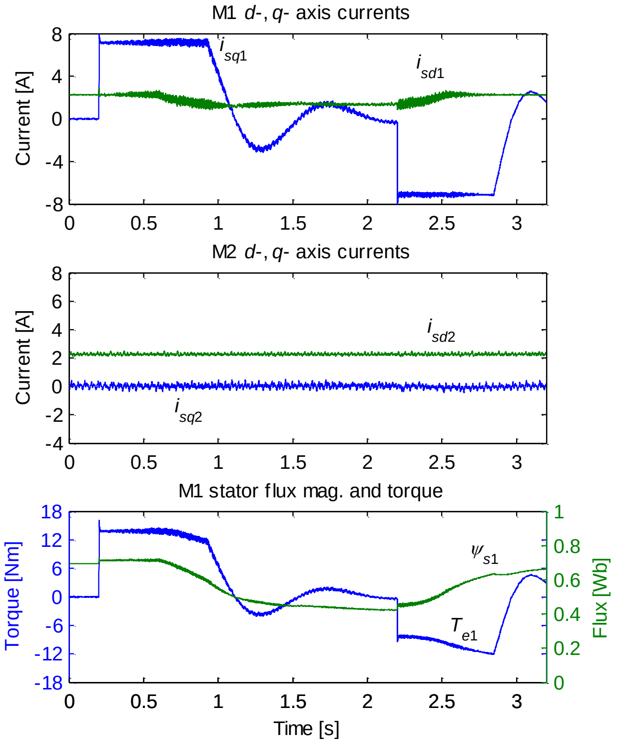

Fig. 16. An improved PI-based FOC scheme with individual field weakening.

other machine's speed in order to decide at what threshold speed field weakening should start for each machine and by how much the *d*-axis current reference needs to decrease (note that in FCS-MPC Mode-III the level of field weakening in the machines is not the same, Fig. 13). The attempts to formulate such a control scheme have not succeeded so far. However, this problem is solved in a rather straightforward manner in the FCS-MPC algorithm (Mode-III), thanks to the MIMO control nature. The experimental results show that Mode-III performance is better than in all the other modes, including the improved FOC scheme.

B. Other Issues

A detailed comparison of transients of M1's flux, torque, and speed traces in Mode-II and Mode-III is conducted next. Zoomed extracts of Figs. 11 and 13 are shown in Fig. 17. A careful inspection reveals that Mode-II gives a slightly slower speed response compared to Mode-III. Upon the activation of the voltage constraint and hence the lowering of ψ_{s1}^* (and ψ_{s2}^* in Mode-III), the model predictive controller attempts to keep T_{e1} at the reference T_{e1}^* (which is not recorded, but can be assumed to be almost the same as the T_{e1}^* trace in Fig. 18, obtained by simulation, since T_{e1}^* only reduces from the imposed maximum value when ω_{r1} crosses ω_{r1}^*), provided by the outer loop's PI speed controller. However, T_{e1} in Mode-II reduces before the instant when T_{e1}^* starts to decrease; this phenomenon has been also verified by simulation (Fig. 18). It is explained by the existence of two field weakening regions. These regions are known in the conventional high-speed field weakening (FW) [11] as active-V&I-constraints (FW-I), where the achievable torque is limited by the imposed current/torque limit (to e.g. the rated torque value, as in this study) and active-V-constraint-only (FW-II), where the achievable torque is reduced due to the voltage limit (increase of torque by increasing of current is no longer feasible). The BSFW operation, experienced in Mode-II, consists of both FW-I, where T_{e1} is maintained at the expense of higher-than-rated current, and FW-II, where T_{e1} has to be reduced below the T_{e1}^*. The voltage related weighting factors have some (but minor) impact on the torque transient reduction in the BSFW region.

Torque tracking with offset should be avoided in this drive topology as it results in torque disturbance at the other machine due to the single cost function. This is evident in the disturbance in T_{e2} trace in Fig. 11 (and would become more severe if T_{e2} were of non-zero value, because the torque errors would be shared by T_{e1} and T_{e2} due to the single cost function with equal torque error weighting). On the other hand, Mode-III operation remains only in the FW-I region because more dc-bus voltage is available to M1; this again shows the superiority of the Mode-III. It must be emphasized that the automatic torque adjustment during field weakening is done internally by the FCS-MPC algorithm without any external intervention.

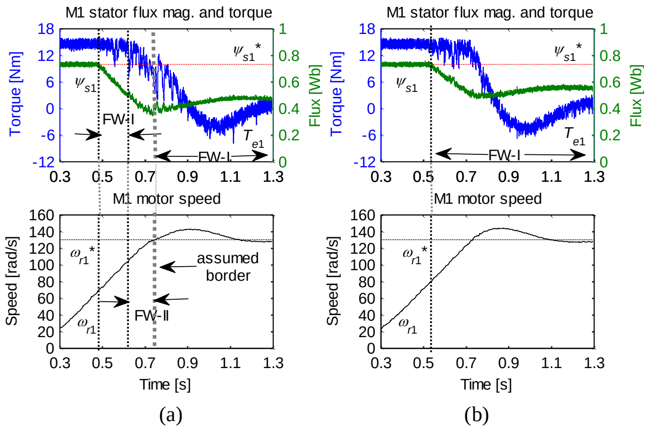

Fig. 17. Zoomed extracts of M1 flux, torque and speed traces of (a) Mode-II operation of Fig. 11 and (b) Mode-III operation of Fig. 13. (The assumed 'border' in the discussion is taken as the instant when ω_{r1} crosses ω_{r1}^*).

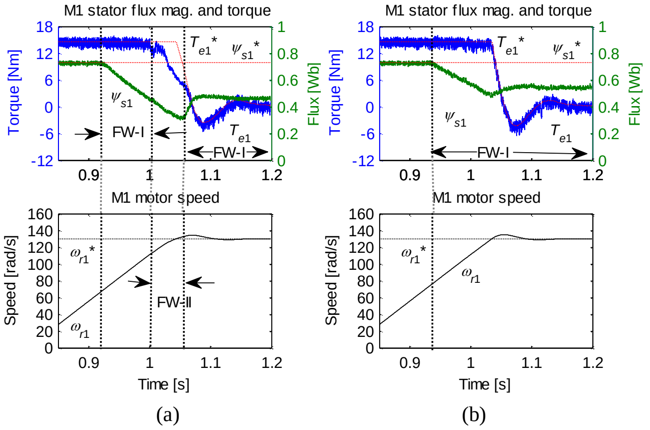

Fig. 18. Corresponding simulation verification of the field weakening regions in Fig. 17: (a) Mode-II operation; (b) Mode-III operation. The same machine parameters (except inertia), dc-bus voltage, and speed references as in the experimental conditions in Fig. 17 are used.

Finally, the maximum achievable torque of the two machines is analyzed. Fig. 19 shows possible speed regions

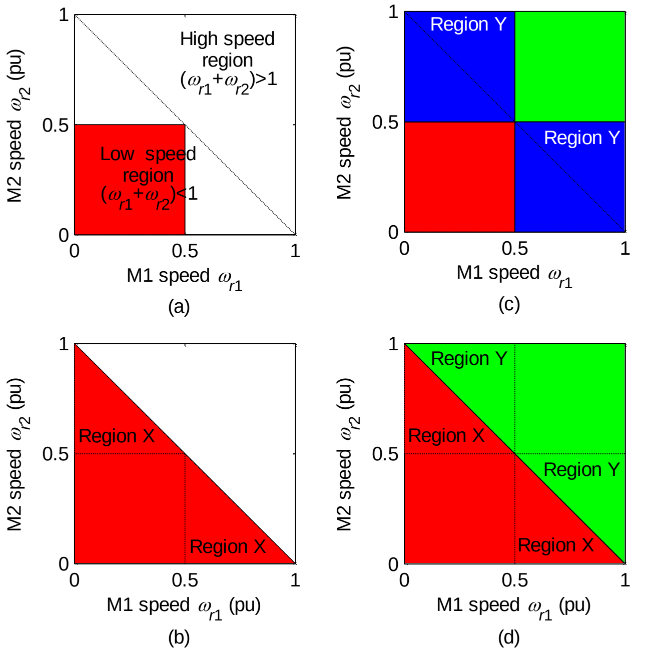

Fig. 19. Speed operating regions and their correlation with the maximum achievable torque (assuming that the drive's current limit does not change and the inverter remains in the linear modulation region) of the two motors controlled by: (a) FOC with equal dc-bus voltage allocation PWM [1]; (b) FCS-MPC Mode-I or FOC with arbitrary dc-bus voltage allocation PWM [2]; (c) FCS-MPC Mode-II or FOC with equal dc-bus voltage allocation PWM [1] and individual machine's field weakening; (d) FCS-MPC Mode-III. Colour coding: White – operation not possible; Red – operation with both machines in the base speed region and full maximum (rated) torque development; Green – both machines operated in BSFW with reduced maximum achievable torque; Blue – either machine in BSFW operation with reduced maximum torque. The speeds are in per-unit system, normalised with respect to the rated value.

of operation of the two machines for all the schemes discussed above and their relationship with the maximum torque achievable (full – i.e. rated, or reduced). Fig. 19(a) shows the conventional FOC scheme with equal dc-bus voltage allocation and no field weakening, while Fig. 19(b) represents the FCS-MPC Mode-I scheme and FOC scheme with arbitrary dc-bus voltage allocation. Fig. 19(c) represents the FCS-MPC Mode-II scheme and the FOC scheme with individual machine field weakening. Finally, Fig. 19(d) shows the operating region of the FCS-MPC Mode-III scheme. Control schemes illustrated in Figs. 19(c) and 19(d) are characterized with significantly wider operating regions than Figs. 19(a) and 19(b). Fig. 19(b) indicates that the corresponding control schemes fully utilize the dc-bus voltage and subsequently extend the maximum (i.e., rated) torque region into areas labeled as Region X, when compared to Fig. 19(a). It should be noted that the FCS-MPC Mode-III also has the advantage of full maximum torque in the Region X by fully utilizing the dc-bus voltage. In contrast to this, Mode-II scheme has a reduced maximum torque in the Region X. In areas labeled as Region Y in Figs. 19(c) and 19(d), for non-zero load torques, both machines are field weakened in Mode-III scheme but only one or the other machine is field weakened in Mode-II scheme. Theoretically, this leads to a lower total current flow in Region Y in Mode-III scheme. All these scenarios have been illustrated by corresponding experimental investigation in the previous section.

VII. CONCLUSION

In the considered fault-tolerant two-motor drive topology the problem of simultaneous post-fault operation of both machines at higher speeds arises. It is shown that the FCS-MPC based flux and torque control scheme with voltage limit consideration not only enables independent machine control, but it also yields an automatic adjustment of the stator fluxes in accordance with the voltage limit of the topology. This is achieved by exploiting the feature of the MPC that enables MIMO control and allows for reference tracking with an offset while properly respecting the imposed voltage constraint.

When one machine requires a higher voltage, the machines are dynamically brought into field weakening region with reduced stator flux magnitude, although the speed is in the base speed region. Three possible control modes are examined. Mode-III is found to be the superior control mode. The resulting performance has been investigated and verified using extensive experimentation.

Developed FCS-MPC schemes have been also compared with the conventional PI-based FOC scheme. It is concluded that model predictive control, owing to its MIMO control and constraint consideration characteristics, does possess some advantages over the PI controllers, especially in a complex drive control problems such as this one.

APPENDIX: MATRICES USED IN (3) AND (4)

Only the first-step prediction requires the accurate prediction of the rotor flux components, in contrast to both steps in [6]. Continuous-time state-space model is given with (3), where

$$\mathbf{A}_t = \mathbf{A}_c + \mathbf{A}_\omega,$$

$$\mathbf{A}_c = \begin{bmatrix} -(\frac{1}{\sigma T_s} + \frac{1-\sigma}{\sigma T_r}) & 0 & \frac{1-\sigma}{\sigma L_m T_r} & 0 \\ 0 & -(\frac{1}{\sigma T_s} + \frac{1-\sigma}{\sigma T_r}) & 0 & \frac{1-\sigma}{\sigma L_m T_r} \\ \frac{L_m}{T_r} & 0 & -\frac{1}{T_r} & 0 \\ 0 & \frac{L_m}{T_r} & 0 & -\frac{1}{T_r} \end{bmatrix},$$

$$\mathbf{A}_\omega = \begin{bmatrix} 0 & 0 & 0 & \frac{\omega_{re}(1-\sigma)}{\sigma L_m} \\ 0 & 0 & -\frac{\omega_{re}(1-\sigma)}{\sigma L_m} & 0 \\ 0 & 0 & 0 & -\omega_{re} \\ 0 & 0 & \omega_{re} & 0 \end{bmatrix},$$

$$\sigma = 1 - \frac{L_m^2}{L_s L_r}, T_s = \frac{L_s}{R_s}, T_r = \frac{L_r}{R_r},$$

$$\mathbf{B}_t = \begin{bmatrix} \frac{1}{\sigma L_s} & 0 \\ 0 & \frac{1}{\sigma L_s} \\ 0 & 0 \\ 0 & 0 \end{bmatrix}$$

Discrete-time state-space model is given with (4), where

$$\mathbf{\Phi}_k = e^{\mathbf{A}_c T} \cdot e^{\mathbf{A}_\omega T}, \quad \mathbf{\Gamma}_k = \int_0^T \left(e^{\mathbf{A}_t \tau} \mathbf{B}_t\right) \cdot d\tau$$

Applying Cayley-Hamilton theorem to obtain an accurate representation of $e^{\mathbf{A}_\omega T}$ in linear algebraic form, the discrete-time coefficient matrices are obtained as,

$$\mathbf{\Phi}_k = \begin{bmatrix} E_{Ac}(1,1) & 0 & E_{Ac}(1,3) & 0 \\ 0 & E_{Ac}(2,2) & 0 & E_{Ac}(2,4) \\ E_{Ac}(3,1) & 0 & E_{Ac}(3,3) & 0 \\ 0 & E_{Ac}(4,2) & 0 & E_{Ac}(4,4) \end{bmatrix}$$
$$\begin{bmatrix} 1 & 0 & \frac{(1-\sigma)}{\sigma L_m}[1-\cos(\omega_{re,k}T)] & \frac{(1-\sigma)}{\sigma L_m}[\sin(\omega_{re,k}T)] \\ 0 & 1 & -\frac{(1-\sigma)}{\sigma L_m}[\sin(\omega_{re,k}T)] & \frac{(1-\sigma)}{\sigma L_m}[1-\cos(\omega_{re,k}T)] \\ 0 & 0 & \cos(\omega_{re,k}T) & -\sin(\omega_{re,k}T) \\ 0 & 0 & \sin(\omega_{re,k}T) & \cos(\omega_{re,k}T) \end{bmatrix}$$

$$\mathbf{\Gamma}_k = \int_0^T \left(e^{\mathbf{A}_t \tau} \mathbf{B}_t\right) \cdot d\tau = \frac{T}{\sigma L_s} \begin{bmatrix} E_{Ac}(1,1) & 0 \\ 0 & E_{Ac}(2,2) \\ E_{Ac}(3,1) & 0 \\ 0 & E_{Ac}(4,2) \end{bmatrix}$$

where E_{Ac} terms are the matrix elements of $e^{\mathbf{A}_c T}$ pre-calculated off-line.

REFERENCES

[1] B. Francois and A. Bouscayrol, “Design and modeling of a five-phase voltage-source inverter for two induction motors,” in *Proc. 8th European Conf. on Power Electronics and Applications EPE*, Lausanne, Switzerland, CD-ROM paper 626, 1999.

[2] D. Dujic, M. Jones, S. N. Vukosavic, and E. Levi, “A general PWM method for a (2*n*+1)-leg inverter supplying *n* three-phase machines,” *IEEE Trans. Ind. Electron.*, vol. 56, no. 10, pp. 4107-4118, 2009.

[3] M. Jones, S. N. Vukosavic, D. Dujic, E. Levi, and P. Wright, “Five-leg inverter PWM technique for reduced switch count two-motor constant power applications,” *IET Electrical Power Applications*, vol. 2, no. 5, pp. 275-287, 2008.

[4] R.R. Errabelli and P. Mutscher, “Fault-tolerant voltage source inverter for permanent magnet drives,” *IEEE Trans. Power Electron.*, vol. 27, no. 2, pp. 500-508, 2012.

[5] M. Pulvirenti, G. Scarcella, G. Scelba, M. Cacciato, A. Testa, “Fault tolerant ac multi-drive system,” *IEEE J. Emerging and Selected Topics*

in Power Electron., d.o.i. 10.1109/JESTPE.2013.2292861 (early access).

[6] H. Miranda, P. Cortés, J. I. Yuz, and J. Rodriguez, "Predictive torque control of induction machines based on state-space models," *IEEE Trans. Ind. Electron.*, vol. 56, no. 6, pp. 1916-1924, 2009.

[7] J. Rodriguez, R. M. Kennel, J. R. Espinoza, M. Trincado, C. A. Silva, and C. A. Rojas, "High-performance control strategies for electrical drives: an experimental assessment," *IEEE Trans. Ind. Electron.*, vol. 59, no. 2, pp. 812-820, 2012.

[8] M. Preindl, and S. Bolognani, "Model predictive direct speed control with finite control set of PMSM drive systems," *IEEE Trans. Power Electron.*, vol. 28, no. 2, pp. 1007-1015, 2013.

[9] C. S. Lim, E. Levi, M. Jones, N. A. Rahim, and W. P. Hew, "A comparative study of synchronous current control schemes based on FCS-MPC and PI-PWM for a two-motor three-phase drive," *IEEE Trans. Ind. Electron.*, vol. 61, no. 8, pp. 3867-3878, 2014.

[10] C. S. Lim, E. Levi, M. Jones, N. A. Rahim, and W. P. Hew, "An improved two-motor three-phase drive using FCS-MPC based flux and torque control with voltage constraint consideration," in *Proc. IEEE Int. Electric Machines and Drives Conf. IEMDC*, Chicago, USA, pp. 201-208, 2013.

[11] F. Briz, A. Diez, M. W. Degner, and R. D. Lorenz, "Current and flux regulation in field-weakening operation," *IEEE Trans. Ind. Appl.*, vol. 37, no. 1, pp. 42-50, 2001.

Chee-Shen Lim (S'10, M'14) received the BEng degree (Hons.) in Electrical Engineering from the University of Malaya, Malaysia in 2009 and the joint-university PhD degree from the University of Malaya and Liverpool John Moores University, UK in 2013. He was a research assistant in Power Energy Dedicated Advanced Centre (UMPEDAC), University of Malaya, Malaysia, and is currently with Experimental Power Grid Centre (EPGC), A*STAR Singapore. His research interests include design and control of electrical drives and other power electronic applications.

Emil Levi (S'89, M'92, SM'99, F'09) received his M.Sc. and PhD degrees from the University of Belgrade, Yugoslavia in 1986 and 1990, respectively. From 1982 till 1992 he was with the Dept. of Elec. Engineering, University of Novi Sad. He joined Liverpool John Moores University, UK in May 1992 and is since September 2000 Professor of Electric Machines and Drives. He served as Co-Editor-in-Chief of the IEEE Trans. on Industrial Electronics from 2009 till 2013. He currently serves as an Editor of the IEEE Trans. on Energy Conversion and as Editor-in-Chief of the IET Electric Power Applications. Emil is the recipient of the Cyril Veinott award of the IEEE Power and Energy Society for 2009.

Martin Jones received his BEng degree (First Class Honours) in Electrical Engineering from the Liverpool John Moores University, UK in 2001. He was a research student at the Liverpool John Moores University from September 2001 till Spring 2005, when he received his PhD degree. Dr Jones was a recipient of the IEE Robinson Research Scholarship for his PhD studies and is currently with Liverpool John Moores University as a Reader. His research is in the area of high performance ac drives.

Nasrudin A. Rahim (M'89–SM'08) received the B.Sc. (Hons.) and M.Sc. degrees from the University of Strathclyde, Glasgow, U.K., and the PhD degree from Heriot–Watt University, Edinburgh, U.K., in 1995. He is currently a Professor with the Faculty of Engineering, University of Malaya, Kuala Lumpur, Malaysia, where he is also the Director of the Power Energy Dedicated Advanced Center (UMPEDAC). Prof. Rahim is a Fellow of the IET, U.K., and the Academy of Sciences Malaysia.

Wooi-Ping Hew (M'06) obtained his BEng and Masters (Electrical) degrees from the University of Technology, Malaysia. He received his PhD from the University of Malaya, Kuala Lumpur, Malaysia in 2000. He is currently a Professor in the Faculty of Engineering, University of Malaya, Kuala Lumpur, Malaysia. Dr. Hew is a Member of IET and a Chartered Engineer. His research interests include electrical drives and electrical machine design.